Nonstationary Phase of the Plio-Pleistocene Asian Monsoon

Steven C. Clemens, David W. Murray, Warren L. Prell

Paleoclimate records indicate that the strength of the Asian summer monsoon is sensitive to orbital forcing at the obliquity and precession periods (41,000 and 23,000 years, respectively) and the extent of Northern Hemisphere glaciation. Over the past 2.6 million years, the timing (phase) of strong monsoons has changed by ~83 degrees in the precession and ~124 degrees in the obliquity bands relative to the phase of maximum global ice volume (inferred from the marine oxygen isotope record). These results suggest that one or both of these systems is nonstationary relative to orbital forcing.

The Asian monsoon is a primary component of the tropical and global climate system (*1, 2*). As such, it's variability and evolution are of great interest to both climate modelers and paleoclimatologists. We used the deep-sea sediment record to examine a 3.5-million-year history of the Indian Ocean monsoon in order to understand how it responds to external forcing (orbitally driven changes in solar radiation) and internal forcing (interaction among the atmosphere, oceans, land surface, and ice sheets).

Insolation for any given latitude and season is modulated by Earth's orbital parameters and can be calculated with great precision for the last 10 million years (*3, 4*). These parameters—orbital eccentricity, axial obliquity, and precession of the equinox—have characteristic periods near 100, 41, and 23 thousand years (ky), respectively. However, virtually all the variance in solar radiation is accounted for by precession and obliquity, with precession dominating variance in low to mid-latitudes (*5*).

Major Plio-Pleistocene changes internal to the climate system include the initiation of Northern Hemisphere (NH) glaciation ~2.6 million years ago (Ma) and the characteristic 100-ky fluctuations of Late Pleistocene ice sheets, which began at ~1.2 Ma (*6–8*). The long-term evolution of global ice volume (inferred from $\delta^{18}O$) affects high-latitude climate directly through changes in the extent and elevation of the ice sheets. These changes in glaciation are accompanied by global-scale changes in sea surface temperature (SST), sea level, vegetation, and land-surface albedo (*9–11*), which provide dynamic links to low-latitude climate systems such as the monsoon. To reconstruct these long-term changes in climate, we rely on proxy indices preserved in the geological record.

Modern monsoon meteorology. Both sensible and latent heating contribute to the temperature and pressure gradients that drive summer monsoon circulation (Fig. 1) (*2, 12*). Differential sensible heating results in low atmospheric pressure over the warm Asian continent during Boreal summer and, at the same time, high pressure over the cold southern subtropical Indian Ocean (SSIO) during Austral winter. If this interhemispheric pressure gradient were forced entirely by the corresponding insolation gradient, then monsoon strength would be essentially constant year to year. The large interannual variability in monsoon strength results from internal dynamics related, in part, to the storage and export of latent heat from the SSIO. Latent heat collected from the SSIO is transported across the equator and released over Asia during precipitation. This heating strengthens the Asian low-pressure cell, the interhemispheric pressure gradient, and monsoon circulation (*2, 12, 13*). Long-term averages suggest that 80 to 90% of the moisture flux into southern Asia originates from the SSIO, providing a strong teleconnection between Southern Hemisphere (SH) ocean-atmosphere dynamics and NH monsoon strength (*14–17*) (Fig. 1).

Latent heat (*LH*) associated with this moisture transport can be estimated from

$$LH = \rho_a C_E L u \Delta q \qquad (1a)$$

$$\Delta q = q_s - q_a = [Q(T_s) - rQ(T_s + \Delta T)] \qquad (1b)$$

where ρ_a is the air density, C_E is the transfer coefficient, L is the latent heat of vaporization, u is the wind speed, Δq and ΔT are the sea-air humidity and temperature differences, q is the specific humidity, r is the relative humidity, T is the temperature, $Q(T)$ is the saturation-specific humidity as a function of T, subscript s represents the value at the sea-air interface, and subscript a the value at a reference level in the atmosphere where flux is constant (*18*).

On a global basis, *LH* (transferred from ocean to atmosphere) is negatively correlated with T_s (*18*). This relation may appear to be counterintuitive considering the Clausius-Clapeyron function, which indicates that evaporation increases with temperature. This trend, however, is true only if u, ΔT, and r are constant (*18*), conditions that rarely occur naturally. If the effects of u and q_a dominate, then *LH* increases with u and decreases with q_a. Indeed, satellite and surface observations document that *LH* is greatest in the trade-wind regions of the winter hemisphere, where u is strong and T_s is low (low q_a, high Δq) (*13, 17–20*). The seasonal and interannual correlation between increased latent heat, decreased SST, and stronger winds in the winter hemisphere (a time of low insolation) (*18*) suggest that, over orbital time scales, *LH* maxima and monsoon maxima should be associated with SH winters characterized by strong atmospheric circulation.

Proxy climate records. Annually, 70%

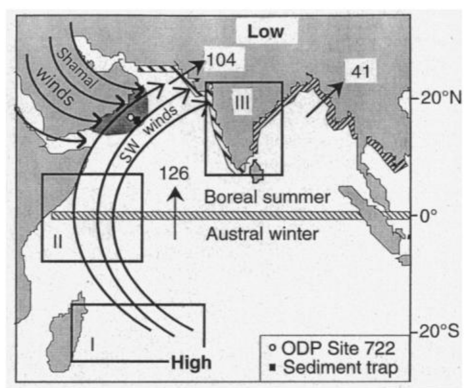

Fig. 1. Site location and summer monsoon dynamics (June to August). Regional winds (arrows) stem from the north-south pressure gradient and cyclonic circulation around the Asian low. The shaded region (northwest Arabian Sea) represents the area of highly productive upwelling driven by southwest summer-monsoon winds and the region of maximal dust deposition from the desert source-areas of Arabia and Somalia. Latent heat transport across hatched boundaries (arrows with numbers) indicate that 87% of the latent heat entering Asia during the summer monsoon season is imported from the southern Indian Ocean (units are in 10^{13} W) (*17*). Time series of anomalies from boxed regions I, II, and III indicate that stronger trade winds and colder SST in the southern Indian Ocean (I) are associated with increased cross-equatorial moisture transport (II) and increased precipitation over India (III) (*13*). Anomalies are relative to the average between 1954 and 1976. Ocean Drilling Program (ODP) Site 722B [16°37′N, 59°48′E, 2028 m below sea level (mbsl)]; Sediment Trap (*21*) (16°19′N, 60°28′E; 3000 mbsl).

The authors are in the Department of Geological Sciences, Brown University, Providence, RI 02912–1846, USA.

of the flux of biologic detritus and 80% of the flux of lithogenic detritus to Arabian Sea sediments are generated during the summer monsoon (*21*) (Fig. 2). This combined sediment flux is preserved at Ocean Drilling Program (ODP) Site 722 in the northwest Arabian Sea (Fig. 1). Thus, sediments accumulated at this site provide a continuous history of changes in monsoon strength and regional aridity (Fig. 3).

The biological indices of monsoon-driven upwelling include the planktonic foraminifer *Globigerina bulloides* as well as the biogenic opal content of the sediments. Typically G. *bulloides* is a subpolar species, but it is abundant in the Arabian Sea and other tropical upwelling regions characterized by seasonally cold, nutrient-rich waters (*22–26*). High biogenic opal content, an indicator of radiolaria and diatom production, has also been directly linked to Arabian Sea upwelling (*21, 27, 28*).

The lithogenic grain size (LGS) of deep-sea sediments is widely used to monitor changes in wind intensity (carrying capacity) over geological time scales (*29*). In Arabian Sea sediments, LGS provides a means of estimating monsoon wind strength, which drives upwelling-induced productivity. This link is reflected in the covariance between LGS, G. *bulloides*, and opal indicators (*23, 30*), as well as in the positive correlation between LGS and the strength of the southwest winds (*31*). Although much of the lithogenic transport takes place in the Shamal winds (*32*) (Fig. 1), the correlation between LGS and southwest winds is not surprising given that both wind systems are directly linked to the strength of the Asian low-pressure cell.

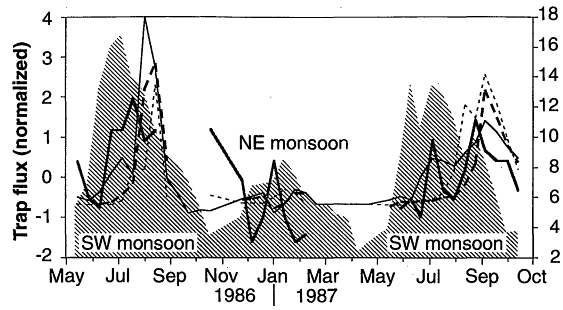

Fig. 2. Sediment trap fluxes associated with summer and winter monsoon circulation. Trap data are normalized for purposes of plotting. Average inputs are shown for peak winter (December through March) and summer (June through September) periods, respectively: *G. bulloides* (light dashed line), 369 and 2071 individuals m^{-2} day^{-1} (*25*); lithogenic flux (light solid line), 16 and 48 mg m^{-2} day^{-1} (*58*); lithogenic grain size (median diameter, volumetric distribution) (heavy solid line), 10.9 and 12.6 μm; and opal flux (heavy dashed line), 13 and 55 mg m^{-2} day^{-1} (*58*). Wind speed (hatched pattern) is shown on the right axis.

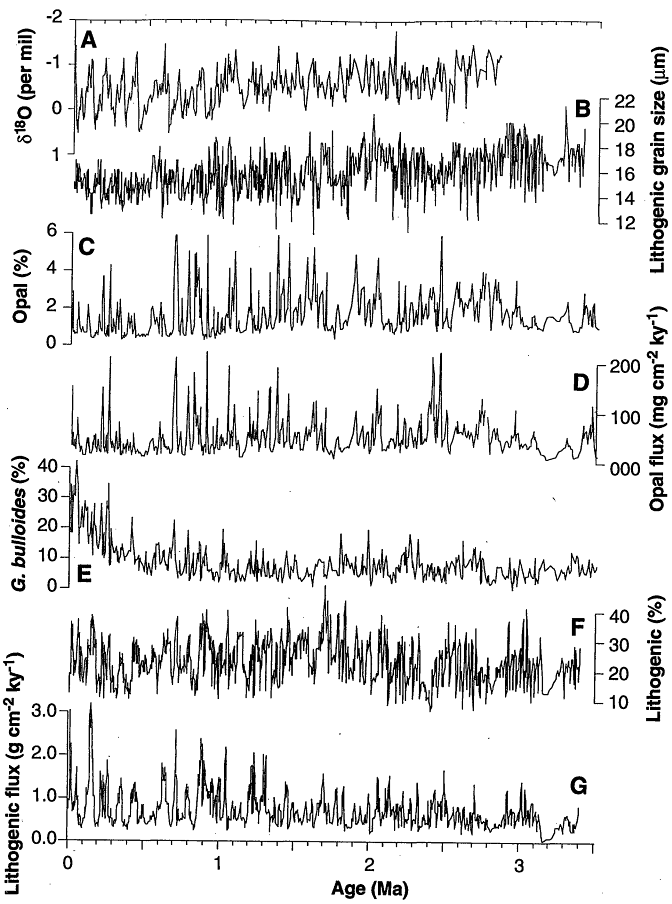

Fig. 3. Proxy climate records from ODP Site 722. (**A**) Global ice volume (δ^{18}O, relative to the Pee Dee belemnite standard), larger values indicate increased glaciation. (**B**) Summer monsoon wind strength (LGS; median diameter, volumetric distribution); larger values are associated with stronger winds. (**C, D,** and **E**) Biological productivity driven by wind-induced upwelling during the summer monsoon (opal %, opal flux, and *G. bulloides* %); larger values indicate increased upwelling. (**F** and **G**), Aridity of desert source areas: Somali and Arabia (lithogenic % and flux); larger values indicate increased aridity. Extraction and analytical methods for the LGS and flux are described in (*30*), for the opal in (*59*) with modifications as in (*27*), for stable isotope analysis in (*60*) except that we used ~11 individual *G. sacculifer* (>150 μm) per analysis, and for *G. bulloides* in (*22*).

Over geologic time scales, the flux of lithogenic material to the oceans is largely unrelated to LGS (*29*). Lithogenic flux depends primarily on aridity in the source area and the extent of glacial climates (*29, 30, 33–35*).

Each proxy indicator is linked to climate variability through quasi-independent pathways in the marine and atmospheric systems. The integrity of each monsoon proxy depends on the extent to which it responds only to monsoon forcing or is influenced by other processes (*23, 27, 30, 36–38*). For example, opal suffers from differential preservation, most apparent in the younger part of the record (*23, 27*), and G. *bulloides* is strongly dissolved in the older part of the record (*38*). Lithogenic grain size responds to wind strength, as well as changes in the deflation potential of the source area. For example, increased vegetation in desert source areas, associated with more pluvial conditions near 9 ka, preclude the grain size proxy from recording the strong monsoon response seen in the opal and G. *bulloides* records (*23, 30, 37*). Our multiproxy approach assumes that the biases associated with each proxy are independent and that the variability in common is the response to monsoon forcing.

Age control for Site 722 samples is constrained by oxygen-isotope stratigraphy, biostratigraphy, and magnetic polarity reversal data (*39*). We developed the Site 722 chronostratigraphy by astronomically tuning lithogenic % to orbital obliquity and precession (*3, 4*). We established the phase relative to orbital forcing by incorporating measured phase differences between lithogenic % and δ^{18}O with the assumption that the phase of global ice volume is constant through time (at Late Pleistocene values) relative to obliquity and precession (*40, 41*). This assumption is critical to understanding the climatic response to external forcing. As such, we separately discuss results that are independent of this assumption (internal to the data set) and those that are not.

Internal phase relations. Our records of monsoon strength, source area aridity, and glacial conditions reveal that high- and low-latitude climates are linked in several ways (Fig. 3). The increased amplitude of the $\delta^{18}O$ and lithogenic flux records after the initiation of 100-ky glaciation cycles (at ~1.2 Ma) reflects a positive relation between high-latitude glaciation and low-latitude aridity (Fig. 3, A and G). The large-amplitude swings in glacial climates of the past 600 ky are reflected in the decreased amplitude of the opal and LGS records of monsoon strength (Fig. 3, B and C). Finally, the long-term decrease in the LGS record parallels the long-term increase in extent of glacial climates (Fig. 3, A and B). Taken together, these observations suggest that the growth of NH ice sheets over the past 3.5 million years weakens the Asian summer monsoon and increases the aridity of subtropical Asia and eastern Africa. These results are consistent with previous studies of the Late Pleistocene interval (*23, 26, 27, 30, 42–44*).

We used an iterative cross-spectral approach to quantitatively evaluate time-dependent coherence and phase relations among climate indices. Coherence is a measure of the linear correlation between two time series over a given frequency band when the phase difference is set to zero. Phase estimates for a given frequency band indicate temporal (lead and lag) relations between variables. Together, coherence and phase parameters allow one to infer physical relations among climate parameters. Because the direct insolation forcing associated with eccentricity is negligible, we concentrated on results from the obliquity and precession bands (*45*) (Fig. 4).

Maxima in the continental aridity records (lithogenic % and flux) are coherent and approximately in phase with glacial maxima ($\delta^{18}O$) over both the precession and obliquity bands (Fig. 4, B and C) (*46*). This

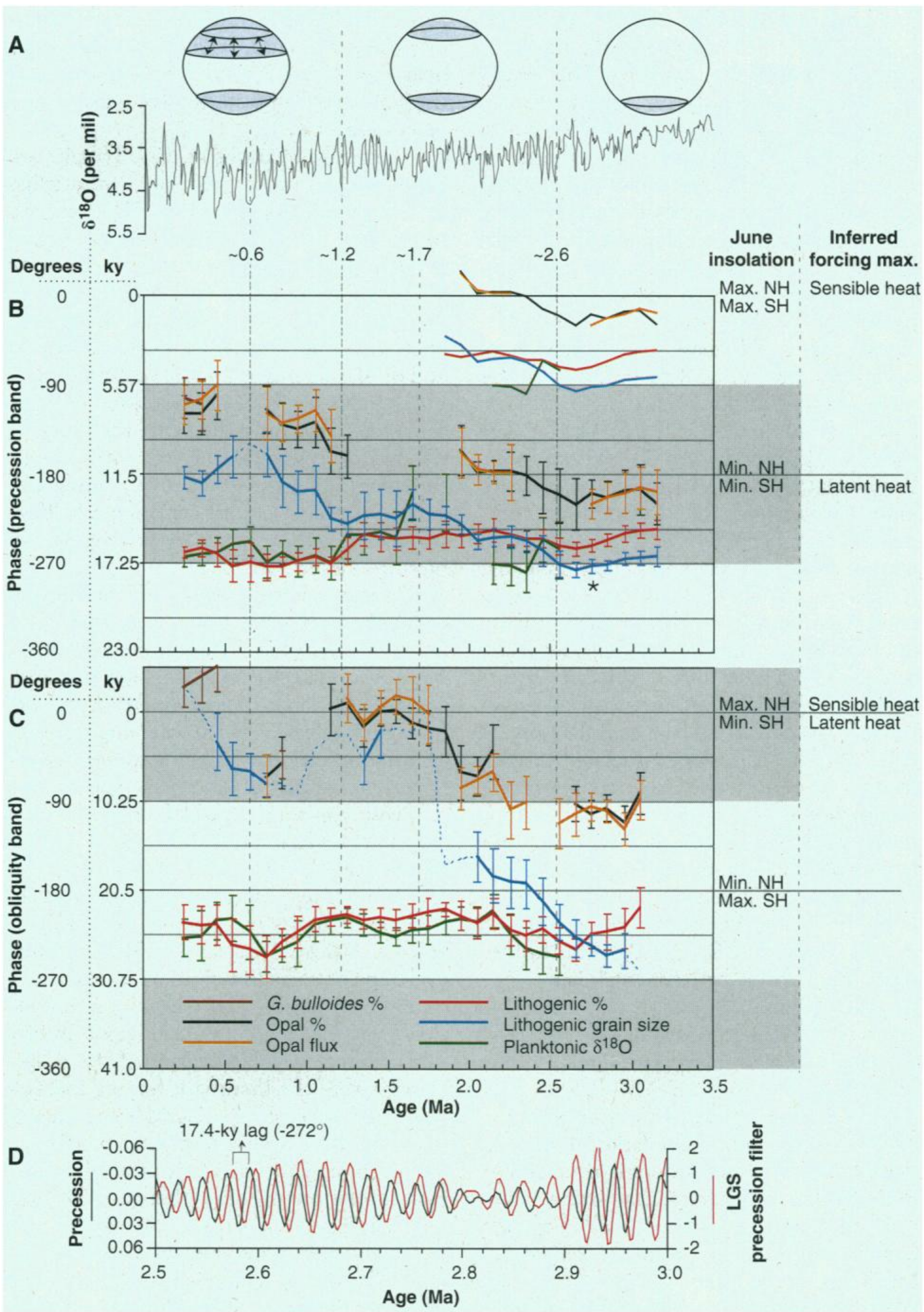

Fig. 4. Coherence and phase relations among indices of glaciation, aridity, monsoon strength, and orbital forcing. (**A**) Site 659 record of global ice volume (*34*) and schematic of northern hemisphere (NH) and southern hemisphere (SH) ice volume through time. At 3.5 Ma, global ice volume was dominated by an East Antarctic ice sheet about two-thirds its modern size, and sea level was ~35 m higher than at present (*11*). Initial growth of significant NH ice sheets is recorded by three isotopically heavy events in the global $\delta^{18}O$ record at ~2.6 Ma. Initiation of 100-ky Ice Age cyclicity in the NH ice sheets occurred at ~1.2 Ma. Amplification of this cyclicity initiated at ~0.6 Ma, resulting in glacial age sea-level drops of 120 m relative to present. (**B** and **C**) Phase plots displaying cross-spectral relations between orbital variations and changes in climate tracers that occur over a given frequency band. Each climate record is compared spectrally (*61*) with the La90 orbital solution (*4*) using a bandwidth of 0.008887 ky^{-1} and a 500-ky window. The analysis window is stepped through the length of each record at 100-ky time steps beginning at 0.25 Ma. The result of each analysis (and the associated error) is plotted at the midpoint of the 500-ky window provided statistical significance exceeds the 80% CI. Results where the CI is <80% are represented by a dashed line or are not plotted. Zero on the *y* axes are set at maximum precession (−Precession; 21 June perihelion) and maximum obliquity, both coinciding with maximum NH summer radiation. *y* axes, 0° to −360°, represent one precession cycle [(B) 23 ky] and one obliquity cycle [(C) 41 ky]. Thus, each point, represented by an error bar, gives the phase of the maximum response of a climate index relative to orbital maxima for a 500-ky interval of time. For example, the LGS data point (*) on the precession plot [(B) coordinates = −272°, 2.75 Ma] indicates that LGS is coherent with orbital precession (>80% CI) and that LGS maxima occur −272° ± 10° (17.4 ± 0.6 ky) after NH summer insolation maxima for the 500-ky interval from 2.5 to 3.0 Ma. (**D**) The time series corresponding to this data point (*). Phase of the lithogenic % and flux records are identical; we show only the percent plot. The phase of the *G. bulloides* record before 1.0 Ma (not plotted) is strongly influenced by dissolution and hence not interpreted as a monsoon index before this time. The thin lines without error bars (B) reflect the scenario in which the Late Pliocene–Early Pleistocene phase of $\delta^{18}O$ is shifted by 180° relative to its Late Pleistocene value as discussed in the text.

result is consistent with previous findings of a positive relation among glacial climates, continental aridity, and atmospheric dust loading (*29, 30, 33, 34, 44, 47*).

Over the precession band, the phase of the monsoon strength indicators (opal and LGS) parallel one another but are consistently offset (Fig. 4B). We assumed that the phase of monsoon maxima resides somewhere between the two indicators, but either one taken alone as the true indicator would not change our conclusions. The phase of both monsoon indicators in the precession band is nonstationary relative to maximum glaciation ($\delta^{18}O$) and aridity (lithogenic % and flux). The phase of monsoon maxima (average of LGS and opal) evolve from −225° to −140° at an average rate of 1° per 31 ky (Fig. 4B). This evolution is coincident with the Plio-Pleistocene growth of NH ice sheets and the extent of glacial climates (Fig. 4A). The timing of slope inflections in the phase plots of the monsoon indices provides further evidence of a coupling between the growth of high-latitude ice volume and Asian monsoon strength. Inflections in the LGS and opal phase plots occur near 2.6, 1.2, and 0.6 Ma. These times also mark the initiation of significant NH ice growth (~2.6 Ma), the initiation of 100-ky cyclicity (~1.2 Ma), and the amplification of the 100-ky Ice Age cycles (~0.6 Ma) (*6–8*). As NH ice sheets and glacial climates expanded, the phase of monsoon maxima shifted toward ice minima (−90° in Fig. 4B). This phase evolution is consistent with general circulation model (GCM) sensitivity tests that indicate weakened Asian monsoons during times of maximum NH glaciation, although the exact processes by which high-latitude ice sheets weakened the monsoon are not well established (*48–50*). The slope inflection at ~1.7 Ma (Fig. 4B) is not associated with an obvious event in the ice-volume record, although it is evident in the stable isotope record of African paleosols, which monitor large-scale changes in vegetation and meteoric waters, and in records of African aridity (*35, 51*). These African records also record events near 2.6, 1.2, and 0.6 Ma, further supporting a link between high- and low-latitude climates.

Over the obliquity band, the phases of the LGS and opal records are similar to one another from 0 to ~1.7 Ma. Before ~1.7 Ma, the LGS is significantly offset from the opal record (Fig. 4C). The bimodal distribution of lithic grain sizes in some samples may indicate that another mechanism, in addition to summer-monsoon wind strength, contributes to LGS variations before 1.7 Ma. Thus, in the interval before 1.7 Ma, we consider the opal record a more reliable monsoon indicator within the obliquity band. As with the precession band, the phase of the monsoon indices in the obliquity band is nonstationary relative to maximum glaciation ($\delta^{18}O$) and aridity (lithogenic % and flux). Here the phase of monsoon maxima evolves from −100° to ~0° at an average rate of 1° per 21 ky (Fig. 4C), paralleling the growth of glacial climates as found for the precession band. Relative to precession, the phase plots for the obliquity band are characterized by stronger inflections in slope and intervals of lower coherence [<80% confidence interval (CI)]. Reduced coherence is consistent with the low- to middle-latitude dominance of precessional over obliquity variance in the insolation forcing (*5*). Inflections in the obliquity phase plots of LGS and opal also occur near 2.6, 1.7, 1.2, and 0.6 Ma, although they are not as well resolved as in the precession plot.

The phase relations discussed above are derived from indices generated from splits of the same samples. These relations are internal to the data set and are thus independent of the assumption that the phase of $\delta^{18}O$ (ice volume) is constant relative to the orbits. However, knowledge of the true phase relation between a climate parameter and orbital forcing is critical to understanding the climatic response to orbital (insolation) forcing. Our finding that the phase of the monsoon is not stationary relative to the phase of glaciation ($\delta^{18}O$) indicates that the phase of one or both of these parameters is nonstationary relative to orbital insolation forcing.

Orbital phase relations: Stationary $\delta^{18}O$ phase. No direct evidence exists for a nonstationary phase relation between Plio-Pleistocene ice volume (a slow-response system with large thermal inertia) and orbital parameters. As such, one might assign all the nonstationarity to the monsoon system, a fast-response atmospheric-ocean system with comparatively little inertia. The *y* axes in the phase plots of Fig. 4, B and C, reflect this scenario (*41*) and suggest the following interpretations. For the precession band, monsoon maxima (LGS, opal, and *G. bulloides*) occur within the hemicycle characterized by minima in both NH summer insolation and SH winter insolation (−90° to −270°; shaded region in Fig. 4B). If direct sensible heating of the Asian plateau were the dominant forcing mechanism, as suggested by GCM experiments (*48–50*), then monsoon maxima would occur in phase with or slightly after NH summer insolation maxima (between 0° and −90° in Fig. 4B). This is clearly not the case; monsoon phase ranges between 90° and 180° out of phase with NH summer insolation maxima. This suggests (i) that the latent and sensible heat mechanisms are uncoupled and (ii) that latent heat maxima are associated with SH insolation minima during Austral winter (~180° in Fig. 4B). These inferences are consistent with monsoon dynamics at the annual and interannual scale (*13, 17, 18*) and with previous Late Pleistocene results (*23*).

In the obliquity band, monsoon maxima (opal and LGS) occur within the hemicycle characterized by both NH summer insolation maxima and SH winter insolation minima (−270° to −90°; shaded region in Fig. 4C). Consistent with our interpretation for precession, this hemicycle is characterized by maxima in latent heat forcing (associated with insolation minima during SH winter) and sensible heat forcing (associated with insolation maxima during NH summer). Thus the sensible and latent heat sources work synchronously to influence the timing of strong monsoons within the obliquity band.

For this scenario, the nonstationary phase of the monsoon stems from its response to both external and internal forcing mechanisms including (i) latent and sensible heating over Asia, fast-response variables that are phase-locked to the orbits before the initiation of NH glaciation, and (ii) the long-term increase in NH ice volume, a slow-response variable internal to the climate system. Before significant NH glaciation, monsoon maxima would presumably be in phase with or slightly lag maximum latent or sensible heating, or both (by <90° for a linear response system). For precession this value would lie between −180° and −270° (Fig. 4B) and for obliquity, between 0° and −90° (Fig. 4C). The development of NH glaciation weakens the monsoon at these equilibrium phases, forcing monsoon maxima earlier and earlier in the precession and obliquity cycles. Several GCM studies have indicated that large-scale vegetation change can significantly affect the climate response to orbital forcing (*52–54*). Thus, one means of weakening the monsoon could be through increased albedo of the Tibetan Plateau as a function of vegetation response to increasing glacial conditions.

Orbital phase relations: Nonstationary $\delta^{18}O$ phase. The observations and interpretations based on holding the phase of $\delta^{18}O$ constant through time are consistent (i) with modern meteorological dynamics in terms of latent and sensible heat sources and (ii) with decreased monsoon strength during more glacial climates as suggested by GCM results and observed in time series relations (Fig. 3). However, in the absence of significant NH glaciation, GCM results suggest that monsoon maxima should respond directly to NH summer insolation. In addition, global ice volume before 2.6 Ma was largely restricted to Antarctica. As such, the ice-volume response to insolation is presumably related to melting during warm SH summers. For the precession band, this interpretation would suggest a $\delta^{18}O$ phase that is 180° different from its Late Pleistocene value. Incorporating this phase into the astronomical tuning would require shifting all the Late Pliocene–Early Pleistocene phase values by 180° (thin lines in Fig. 4B; timing of the 180° shift is completely arbitrary). In this scenario, interpretation of the response to external and internal forcing within the Late Pliocene–Early Pleistocene would be considerably different. Within this interval, monsoon maxima lag NH summer insolation maxima by <90°, a phase relation that is more consistent with GCM results. This interpretation is also broadly consistent with that of deMenocal and co-workers, who tuned maxima in monsoon indices directly to maxima in NH summer insolation between 5.5 and 5.9 Ma, assuming direct insolation forcing of Asian monsoon strength before 2.8 Ma (*35*, *44*).

For the Late Pleistocene portion of the record (~1.2 to 0 Ma), where the phase of $\delta^{18}O$ relative to orbital forcing is well established, our results indicate that monsoon maxima are not a direct response to NH summer insolation within the precession band, suggesting a strong sensitivity to the extent of glacial conditions and latent heating (*23*). However, for the Late Pliocene–Early Pleistocene interval, a range of plausible scenarios can be considered depending on whether or not the phase of $\delta^{18}O$ is stationary relative to orbital forcing. The nonstationary response of the monsoon relative to glaciation and the potential shift in $\delta^{18}O$ phase relative to precession carry implications regarding our capacity to understand the climate response to external forcing on a much broader scale.

Implications for astronomical chronostratigraphy. The expansion of Late Pleistocene ice sheets produces climate change on a global scale. Thus, climate variables other than the monsoon may also exhibit nonstationary phase relations over the past several million years. This inference has important implications for astronomical chronostratigraphy. In this approach, one can date a sedimentary section by directly aligning (or tuning) orbital-scale variations in parameters such as gamma-ray attenuation porosity estimates (GRAPE), magnetic susceptibility, or reflectance data with variations in orbital precession, obliquity, or insolation. Parameters such as GRAPE are used because measurements are automated, producing fast, cost-effective, and highly resolved records. The phase of these variables relative to the orbits is set at the measured Late Pleistocene value (when $\delta^{18}O$ control is available) and often held constant [for example, (*55*)]. Indeed, this procedure has been used to revise radiometric dates for the geomagnetic polarity time scale by up to several hundred thousand years (*55*). However, to understand the climate response to orbital forcing, one must establish the phase of climate indices relative to precession and obliquity to within a few thousand years. If the climate index chosen for tuning at a specific site is nonstationary in phase, the tuning process described above will remove the nonstationary component, producing an inaccurate phase relative to the orbits and relative to climate records from other regions. This undetected nonstationary phase will result in an inaccurate interpretation of the climate-system physics. Thus, tuning parameters must be directly compared to $\delta^{18}O$ to document stationarity or to compensate for nonstationary phase relations. This procedure will enable reliable comparison of phase relations among variables from globally distributed sites (the $\delta^{18}O$ stratigraphy is globally correlative). However, until the phase relation between $\delta^{18}O$ and orbital parameters is established prior to the Late Pleistocene, the physics of the climate response to orbital forcing will remain unresolved.

REFERENCES AND NOTES

1. S. Hastenrath, in *Climate Dynamics of the Tropics*, A. Berger, P. J. Crutzen, H.-W. Georgii, P. V. Hobbs, A. Hollingsworth, Eds. (Kluwer, Boston, 1991), vol. 8, pp. 182–197.
2. P. J. Webster, *Rev. Geophys.* **32**, 427 (1994).
3. J. Laskar, *Icarus* **88**, 266 (1990).
4. ———, F. Jouzel, F. Boudin, *Astron. Astrophys.* **270**, 522 (1993).
5. A. Berger, M.-F. Loutre, C. Tricot, *J. Geophys. Res.* **98**, 10 (1993).
6. N. J. Shackleton *et al.*, *Nature* **307**, 620 (1984).
7. M. E. Raymo, in *Start of a Glacial*, G. J. Kukla and E. Went, Eds. (Springer-Verlag, Berlin, 1992), vol. 13, pp. 207–223.
8. J. Chen, J. W. Farrell, D. W. Murray, W. L. Prell, *Paleoceanography* **10**, 21 (1995).
9. CLIMAP (Geological Society of America, Boulder, CO, 1981).
10. COHMAP Members, *Science* **241**, 1043 (1988).
11. H. Dowsett *et al.*, *Global Planet. Change* **10**, 169 (1994).
12. P. J. Webster, *The Elementary Monsoon*, J. S. Fein and P. L. Stephens, Eds. (Wiley, New York, 1987).
13. D. L. Cadet and B. C. Diehl, *Mon. Weather Rev.* **112**, 1921 (1984).
14. D. Hastenrath and P. J. Lamb, *J. Phys. Oceanogr.* **10**, 694 (1980).
15. D. Cadet and G. Reverdin, *Tellus* **33**, 476 (1981).
16. D. L. Cadet and S. Greco, *Mon. Weather Rev.* **115**, 2358 (1987).
17. S. Hastenrath and L. Greischar, *J. Geophys. Res.* **98**, 6869 (1993).
18. T. W. Liu, A. Zhang, J. K. B. Bishop, *ibid.* **99**, 12 (1994).
19. S. Hastenrath and P. J. Lamb, *Climatic Atlas of the Indian Ocean*, part 2, *The Oceanic Heat Budget* (Univ. of Wisconsin Press, Madison, WI, 1979).
20. ———, *Climatic Atlas of the Indian Ocean*, part 1, *Surface Climate and Atmospheric Circulation* (Univ. of Wisconsin Press, Madison, WI, 1979).
21. R. R. Nair *et al.*, *Nature* **338**, 749 (1989).
22. W. L. Prell, in *Climate Processes and Climate Sensitivity*, J. Hansen and T. Takahashi, Eds. (American Geophysical Union, Washington, DC, 1984), vol. 29, pp. 48–57.
23. S. C. Clemens, W. L. Prell, D. Murray, G. Shimmield, G. Weedon, *Nature* **353**, 720 (1991).
24. L. C. Peterson, J. T. Overpeck, N. G. Kipp, J. Imbrie, *Paleoceanography* **6**, 99 (1991).
25. W. B. Curry, D. R. Ostermann, M. V. S. Guptha, V. Ittekkot, in *Upwelling Systems: Evolution Since the Early Miocene*, C. P. Summerhayes, W. L. Prell, K. C. Emeis, Eds. (Geological Society of London, London, 1992), pp. 93–106.
26. D. M. Anderson and W. L. Prell, *Paleoceanography* **8**, 193 (1993).
27. D. W. Murray and W. L. Prell, in (*25*), pp. 301–322.
28. B. Haake *et al.*, *Deep-Sea Res.* **40**, 1323 (1993).
29. D. K. Rea, *Rev. Geophys.* **32**, 159 (1994).
30. S. Clemens and W. L. Prell, *Paleoceanography* **5**, 109 (1990).
31. L. M. Nik and S. C. Clemens, *Eos Trans. Am. Geophys. Union* **76**, OS5 (1996).
32. F. Sirocko and M. Sarnthein, in *Palaeoclimatology and Palaeometeorology: Modern and Past Patterns of Global Atmospheric Transport*, M. Leinen and M. Sarnthein, Eds. (Kluwer, Boston, 1989), vol. 282, pp. 401–434.
33. S. A. Hovan, D. K. Rea, N. G. Pisias, N. J. Shackleton, *Nature* **340**, 296 (1989).
34. R. Tiedemann, M. Sarnthein, N. J. Shackleton, *Paleoceanography* **9**, 619 (1994).
35. P. B. deMenocal and J. Bloemendal, in *Paleoclimate and Evolution with Emphasis on Human Origins*, E. S. Vrba, G. H. Denton, T. C. Partridge, L. H. Burckle, Eds. (Yale Univ. Press, New Haven, CT, 1995), pp. 262–288.
36. S. C. Clemens, thesis, Brown University, Providence, RI (1990).
37. ——— and W. L. Prell, *J. Geophys. Res.* **96**, 22 (1991).
38. W. L. Prell, D. W. Murray, S. C. Clemens, D. M. Anderson, in *The Indian Ocean: A Synthesis of Results from the Ocean Drilling Program*, R. A. Duncan, D. K. Rea, R. B. Kidd, U. Von Rad, J. K. Weissel, Eds. (American Geophysical Union, Washington, DC, 1992), vol. 70, pp. 447–469.
39. W. L. Prell, N. Nütsuma, P. A. Meyers, K.-C. Emeis, Eds., *Proc. ODP Sci. Results* (Ocean Drilling Program, College Station, TX, 1991), vol. 117.
40. J. Imbrie *et al.*, in *Milankovitch and Climate*, part 1, A. L. Berger, J. Imbrie, J. Hays, G. Kukla, B. Saltzman, Eds. (Riedel, Boston, 1984), pp. 269–305.
41. Lithogenic % was used as the tuning parameter because it has twice the temporal resolution of the $\delta^{18}O$ record and contains a well-resolved precession signal. Phase between $\delta^{18}O$ and lithogenic % was established by cross-spectral analysis. We found no evidence of discrete phase shifts between lithogenic % or flux and $\delta^{18}O$ over the past 3.5 Ma at Site 722. This result agrees with those previously published for Site 659 over the interval 0.5 to 3.5 Ma (*34*). Our analysis suggests a zero phase relation at the precession band and a ~2-ky lead over the obliquity band. Retaining the phase of ice at Late Pleistocene values relative to orbits (*40*) (6-ky lead for precession, 11.4-ky lead for obliquity), we constructed a tuning target by normalizing tilt and precession (*3*–*4*), applying the measured phase relations (11.4 + 2 = 13.4 ky for obliquity and 6 + 0 = 6 ky for precession), and averaging the two records. Site 722 lithogenic % maxima were then correlated directly to maxima in the tuning target.
42. W. L. Prell, in (*40*), pp. 349–366.
43. G. B. Shimmield, S. R. Mowbray, G. P. Weedon, *Trans. R. Soc. Edinburgh* **81**, 289 (1990).
44. P. B. deMenocal, *Science* **270**, 53 (1995).
45. Our analysis of the eccentricity band yielded no interpretable results with respect to monsoon strength although some Late Pleistocene records indicate significant concentrations of variance at the 100-ky band (*26*, *56*, *57*). Our findings regarding regional aridity differ little from previously published results (*29*, *30*, *33*–*35*, *47*).

46. The same is found for benthic $\delta^{18}O$. We present the planktonic record because it has better coherence with orbital precession and with the lithogenic % and flux records. Carbonate dissolution prevents development of a continuous $\delta^{18}O$ record (*G. sacculifer*) from 2.85 to 3.5 Ma. However, lithogenic % and $\delta^{18}O$ data (*G. sacculifer*) over the intervals 3.4 to 3.73 Ma and 4.2 to 4.5 Ma indicate in-phase relations.
47. S. C. Clemens and W. L. Prell, in *Proc. ODP Sci. Results*, W. L. Prell, N. Niitsuma, P. A. Meyers, K.-C. Emeis, Eds. (Ocean Drilling Program, College Station, TX, 1991), vol. 117, pp. 365–388.
48. J. E. Kutzbach and P. J. Guetter, *J. Atmos. Sci.* **43**, 1726 (1986).
49. W. L. Prell and J. E. Kutzbach, *Nature* **360**, 647 (1992).
50. P. B. deMenocal and D. Rind, *J. Geophys. Res.* **98**, 7265 (1993).
51. T. E. Cerling, J. R. Bowman, J. R. O'Neil, *Palaeogeogr. Palaeoclimatol. Palaeoecol.* **63**, 335 (1988).
52. F. A. Street-Perrott, J. F. B. Mitchell, D. S. Marchand, J. S. Btunner, *Trans. R. Soc. Edinburgh Earth Sci.* **81**, 407 (1990).
53. G. B. Bonan, D. Pollard, S. L. Thompson, *Nature* **359**, 716 (1992).
54. J. A. Foley, J. E. Kutzbach, M. T. Coe, S. Levis, *ibid.* **371**, 52 (1994).
55. N. J. Shackleton, S. Crowhurst, T. Hagleberg, N. G. Pisias, D. A. Schneider, in *Proc. ODP Sci. Results* (Ocean Drilling Program, College Station, TX, 1995), vol. 138, p. 73–101.
56. K.-C. Emeis, D. M. Anderson, H. Doose, D. Kroon, D. Schulz-Bull, *Quat. Res.* **43**, 355 (1995).
57. M. A. Altabet, R. Francois, D. W. Murray, W. L. Prell, *Nature* **373**, 506 (1995).
58. P. Schafer and V. Ittekkot, *Naturwissenschaften* **80**, 511 (1993).
59. R. A. Mortlock and P. N. Froelich, *Deep-Sea Res.* **36**, 1415 (1989).
60. J. W. Farrell and T. R. Janecek, in *Proc. ODP Sci. Results*, J. Peirce and J. Weissel, Eds. (Ocean Drilling Program, College Station, TX, 1991), vol. 121, pp. 297–355.
61. G. M. Jenkins and D. G. Watts, *Spectral Analysis and Its Applications* (Holden Day, Oakland, 1968).
62. Supported by the Ocean Science Division of the NSF and JOI/USSSP. Samples were provided by the international Ocean Drilling Program. Technical assistance was provided by L. Nik, J. Cook, and A. Martin. We thank F. Sirocko and R. Tiedemann for valuable comments and constructive criticisms.

2 July 1996; accepted 13 September 1996

Structure of the MDM2 Oncoprotein Bound to the p53 Tumor Suppressor Transactivation Domain

Paul H. Kussie, Svetlana Gorina, Vincent Marechal, Brian Elenbaas, Jacque Moreau, Arnold J. Levine, Nikola P. Pavletich*

The MDM2 oncoprotein is a cellular inhibitor of the p53 tumor suppressor in that it can bind the transactivation domain of p53 and downregulate its ability to activate transcription. In certain cancers, MDM2 amplification is a common event and contributes to the inactivation of p53. The crystal structure of the 109-residue amino-terminal domain of MDM2 bound to a 15-residue transactivation domain peptide of p53 revealed that MDM2 has a deep hydrophobic cleft on which the p53 peptide binds as an amphipathic α helix. The interface relies on the steric complementarity between the MDM2 cleft and the hydrophobic face of the p53 α helix and, in particular, on a triad of p53 amino acids—Phe^{19}, Trp^{23}, and Leu^{26}—which insert deep into the MDM2 cleft. These same p53 residues are also involved in transactivation, supporting the hypothesis that MDM2 inactivates p53 by concealing its transactivation domain. The structure also suggests that the amphipathic α helix may be a common structural motif in the binding of a diverse family of transactivation factors to the TATA-binding protein–associated factors.

The p53 tumor suppressor helps maintain the genomic integrity of the cell as it coordinates the cellular response to DNA damage by inducing cell cycle arrest (*1*) or apoptosis (*2, 3*). Accordingly, inactivation of p53 is one of the most common events in neoplastic transformation. In about half of all cancer cases, p53 is inactivated by mutations and other genomic alterations (*4*), and in many of the remaining cases it is functionally inactivated by the binding of the cellular MDM2 oncoprotein, which was originally identified as an amplified gene in a transformed mouse cell line (*5–7*).

p53 can bind to specific DNA sequences (*8*) and activate gene expression (*9*), and this activity of p53 is likely to be central to its growth and suppressing effects because tumor-derived mutants are defective in DNA binding (*8–10*). In normal cells, MDM2 and p53 form a negative feedback loop that helps to limit the growth-suppressing activity of p53 (*11*). In response to DNA damage, which leads to an increase in p53 (*1*), p53 can activate expression of the MDM2 gene (*11*). The MDM2 protein, in turn, can bind the transactivation domain of p53, inhibiting further p53 activity as a transcription factor (*6, 11, 12*). Deletion of MDM2 is lethal to mouse embryos, but transgenic mice lacking both MDM2 and p53 are viable (*13*), suggesting that the downregulation of the growth-suppressing effects of p53 is a key activity of MDM2.

In tumors, gene amplifications and other alterations can result in elevated MDM2 and lead to the constitutive inhibition of p53. Amplification of MDM2 has been observed in more than one-third of soft tissue sarcomas (*7, 14*) and, less often, in other cancers, including glioblastomas (*15*), leukemias (*16*), esophageal carcinomas (*17*), and breast carcinomas (*18*). Tumors harbor-

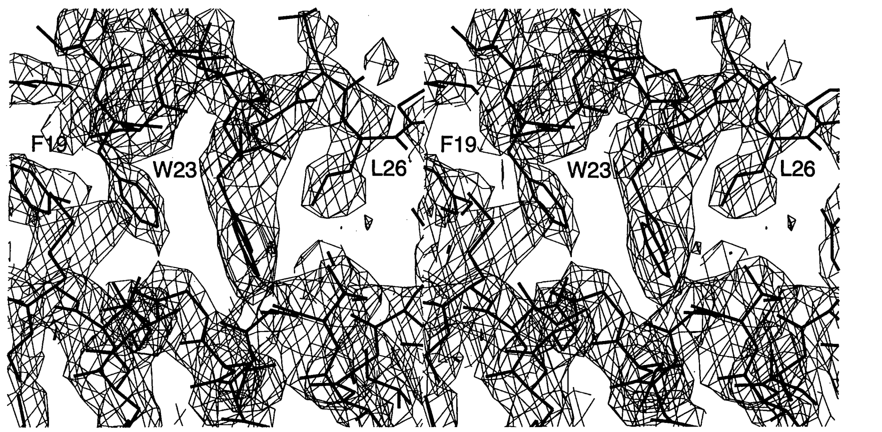

Fig. 1. MIR electron density map of the *X. laevis* MDM2-p53 interface at 3.0 Å resolution, contoured at 1.0 σ, with the refined 2.3 Å resolution atomic model in a stick representation. Stereo view focuses on the interactions of Phe^{19}, Trp^{23}, and Leu^{26} of p53 (labeled) with the $\alpha 2$ helix of MDM2.

P. H. Kussie, S. Gorina, and N. P. Pavletich are with the Cellular Biochemistry and Biophysics Program, Memorial Sloan-Kettering Cancer Center, New York, NY 10021, USA.
V. Marechal is with the Cervice de Microbiologie, Hopital Rothschild, F-75571, Paris 12, France.
B. Elenbaas and A. J. Levine are in the Department of Molecular Biology, Princeton University, Princeton, NJ 08544, USA.
J. Moreau is at the Institut Jacque Monad, Equipe d'Embryologie, 75251, Paris, France.
*To whom correspondence should be addressed. E-mail: nikola@xray2.mskcc.org